Case Studies in Construction Materials 23 (2025) e05165

Contents lists available at ScienceDirect

Case Studies in Construction Materials

journal homepage: www.elsevier.com/locate/cscm

Characterization of steel corrosion in alkali-activated mortars using advanced techniques

Nina Gartner *, Miha Hren, Tadeja Kosec, Andraž Legat

Slovenian National Building and Civil Engineering Institute, Dimičeva ulica 12, Ljubljana 1000, Slovenia

ARTICLE INFO

Keywords:
Corrosion
Alkali-activated mortars
Coupled multi-electrode array (CMEA)
Electrical resistance (ER) sensor
X-ray computed microtomography (microCT)
Visual analysis

ABSTRACT

Alkali-activated materials have emerged as a promising substitute for ordinary Portland cement (OPC) in various applications. This study explores the use of different monitoring techniques for assessing the long-term corrosion behavior of steel in alkali-activated mortars, which remains relatively understudied. Three types of alkali-activated mortars (AAMs) were prepared, based on fly ash, slag, or metakaolin as the precursor material. The corrosion of embedded steel was investigated under wetting and drying cycles with chloride-containing solution for up to one year. Two unconventional techniques were used to monitor corrosion: coupled multi-electrode array sensors (CMEA) to measure partial currents, and electrical resistance (ER) sensors to track thickness reduction. The ER sensors enabled evaluation of general corrosion rates over time, while CMEA provided insight into corrosion initiation and its spatiotemporal distribution. In addition, the corrosion damage on the embedded steel and sensors was evaluated using X-ray computed microtomography (microCT). Distinct corrosion patterns were observed depending on the precursor material: severe corrosion in metakaolin-based AAMs, localized pitting in slag-based AAMs, and moderate damage in fly ash-based AAMs. The study demonstrates the complementary value of CMEA and ER sensors and highlights the challenges of characterizing the long-term corrosion processes in these alternative binder systems

1. Introduction

Concrete, renowned as the most prevalent engineering material, owes its popularity to its cost-effectiveness and adaptability across various environmental settings. However, the primary component in concrete, ordinary Portland cement (OPC), has been contributing a significant 5–8 % of global anthropogenic CO_2 emissions every year during its production [1,2]. This environmental concern has led to the exploration of alternative cementitious materials, such as blended cements, where OPC is partially replaced with supplementary cementitious materials (SCMs), and alkali-activated materials (AAMs), where alkali-activated aluminosilicate precursors serve as a complete substitute for OPC [3,4]. The sustainability of these materials is closely connected with the regional availability of SCMs (e.g. fly ash, slags, and calcined clays) and the optimal use of alkali activators (e.g. sodium hydroxide) [5]. While AAMs do not entirely replace OPC-based concretes, their extensive combinatorial possibilities offer tailored materials with advanced properties for specific applications [6–8].

Recent studies have investigated reinforced alkali-activated systems with recycled materials, showing promising mechanical and durability performance [9,10]. Additionally, research on fiber-modified recycled aggregate concrete has provided insights into its

* Corresponding author.
E-mail address: nina.gartner@zag.si (N. Gartner).

https://doi.org/10.1016/j.cscm.2025.e05165
Received 13 May 2025; Received in revised form 21 July 2025; Accepted 10 August 2025
Available online 11 August 2025

mechanical behavior and damage evolution under various loading conditions [11,12]. However, the adoption of AAMs in reinforced concrete components introduces the possibility of steel corrosion, a primary contributor to reduced structural durability. In conventional OPC-based reinforced concrete structures, steel corrosion is primarily driven by concrete carbonation and the ingress of chloride ions [2]. The corrosion processes in steel exposed to solid cementitious materials, including AAMs, exhibit distinct characteristics. The porous structure of these materials localizes anodic and cathodic sites, affecting electrolyte and oxygen transport within the material [13,14]. Consequently, the assessment of corrosion rates in concrete must include information on the corrosion type, i.e., whether it is uniform across the surface or localized. Additionally, pore solutions in AAMs differ significantly from those in OPC-based concrete due to variations in their chemical composition, mineralogical, and redox properties [15,16]. These distinctions, particularly in high-Ca AAMs using blast furnace slags, can significantly impact the detection of steel corrosion processes within AAMs and make the interpretation of electrochemical parameters more difficult [15,17]. Nowadays, conventional electrochemical techniques are commonly employed to differentiate between the passive and active states of steel embedded in AAMs, and in certain cases also to assess the general corrosion rate [18–21]. On the other hand, information about the localization and dynamics of corrosion processes are rather limited. In our previous studies [22,23], electrochemical techniques applied in AAM mortars and pore solutions were combined with a detailed examination of the steel surface at the end of the experiments. A general correlation between the results obtained by the different methods was established, but it also revealed that conventional electrochemical techniques alone cannot capture the specific characteristics of localized corrosion.

The aforementioned observations have also been reported in the case of corrosion in OPC-based materials, especially in blended cements [14,24,25]. To overcome the deficiencies of conventional electrochemical techniques, various monitoring methods have been developed to facilitate the continuous evaluation of corrosion [26]. One of these methods employs electrical resistance (ER) sensors to quantify corrosion in terms of the reduction in the thickness of the sensors [27,28]. Its successful application in concrete [29] and bentonite [30] has showed its accuracy in evaluating cumulative corrosion damage on metals in porous materials. Another technique, using coupled multi-electrode arrays (CMEAs), represents an advancement of the electrochemical noise (EN) technique [31,32]. CMEAs enable the separate measurement of anodic (corrosion) and cathodic currents, thus permitting the corrosion pattern to be monitored and the corrosion rate assessed over time [33]. In addition to specific corrosion monitoring methods, various microscopic techniques and X-ray computed microtomography (microCT) have proven valuable for assessing actual corrosion damage on steel in concrete (including AAMs) and validating the results obtained through different corrosion monitoring techniques [22,29,34]. Due to the complementary benefits of individual techniques, a combination of conventional electrochemical methods, advanced techniques (ER and CMEA sensors), and visual assessment (microCT) has been successfully studied in our previous research on steel corrosion processes in specific blended cements [28,35]. It was established that corrosion in the blended cements initiated earlier than in the OPC; however, the later evolution of the corrosion rate was generally slower compared to the OPC. Moreover, corrosion in OPC was fairly localized, while in the blended cements it tended to be more uniformly distributed.

Based on our experience with OPC-based materials which showed that information on general corrosion rate and overall corrosion damage is insufficient for a comprehensive understanding of corrosion processes, a similar approach was used to upgrade our previous studies on AAMs. This paper aims to characterize the corrosion processes (initiation and propagation) in AAM mortars composed of steel slag, metakaolin, and fly ash, focusing on the assessment of corrosion rates and distinguishing between different corrosion types in time. To achieve this, two advanced corrosion monitoring techniques, CMEA and ER sensors, were employed. Additionally, visual inspection methods and X-ray computed microtomography (microCT) served as complementary tools to validate the results of long-term monitoring.

2. Materials and methods

2.1. Mortar mix-designs

The alkali-activated mortars (AAMs) employed in this investigation were formulated in accordance with the recipe by RILEM TC 247-DTA [36–39], using three precursor materials: fly-ash (FA8), metakaolin (MK2), and steel slag (S3a-661). The chemical compositions of all materials, determined by XRF or ICP-OES, along with their basic physical properties (d_{50}, BET surface area, and density), are provided in the first RILEM TC 247-DTA publication [36]. The exact same raw materials and original names (FA8, MK2, and

Table 1
Components of the mortar mix-designs [22].

Components [g]	Mortars		
	FA8	MK2	S3a-661
Fly ash (V−378/14)	455.9	-	-
Slag (V−138/15)	-	-	557.4
Metakaolin (V−63/15)	-	450.0	-
Water glass (V−25/15)	168.5	-	22.4
Water glass (V−502/14)	-	372.0	-
NaOH (V−44/15)	-	37.8	33.4
NaOH solution 41.7 % (wt.) NaOH + 58.3 % (wt.) H_2O	64.4	-	-
Tap water	17.7	5.0	232.3
CEN Standard sand (EN 196–1)	1350.0	1350.0	1350.0

S3a-661) of the RILEM TC 247-DTA mortar mixes and their designations were used in this paper. Mortar was selected over concrete due to specimen size limitations imposed by the CMEA and microCT techniques, which required a reduced cover thickness and the exclusion of coarse aggregates. Further details of the mix design for these mortars (Table 1) can be found in our previous publications [22,23].

2.2. Properties of the steels

In this study, various different specimens were prepared, each designed for the specific monitoring technique employed (Fig. 1). Due to the different sizes, geometry, and spatial arrangements of steel, these specimens featured different steel types and shapes, including the surface of two B 500B steel reinforcing bars (with diameters of Φ6 mm and Φ14 mm), a cross-section of the steel wire (diameter 0.50 mm) used for the coupled multi-electrode array (CMEA) sensors, and the surface of a steel sheet etched into the steel conductor of an electrical resistance (ER) sensor.

The chemical composition of all the steels was selected to resemble that of B 500B reinforcing steel, but some variations were detected through optical emission spectroscopy using a SpectroMAXx instrument (Spectro Ametek, UK, 2011), especially with respect to the concentration of carbon (C), as shown in Table 2. Additionally, microstructural differences were observed, which can be attributed to the distinct production processes used for the bars, wire, and sheet. The corrosion properties of steel are influenced by several microstructural factors, including the type of surface exposed (e.g. a cross-section vs. the outer surface), the size and shape of the steel components (e.g. fine or coarse granular structures [40]), and the presence of surface oxides. The corrosion is also influenced by the steel–concrete interface (SCI) [41,42], which is easier to control in CMEA sensors due to their smaller exposed area compared to steel bars.

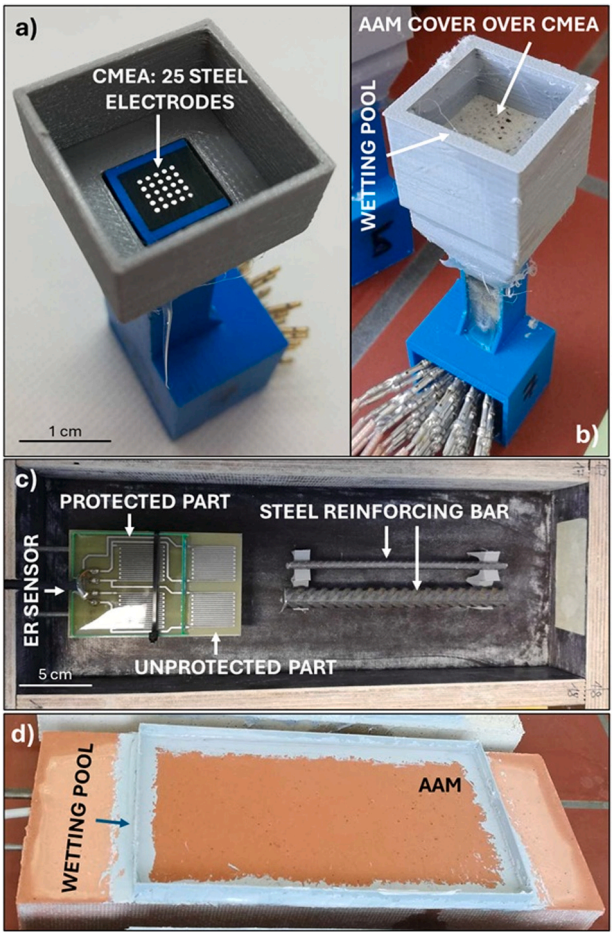

Fig. 1. Configuration of specimens, showing: a) layout of the CMEA sensor before casting, b) specimen with CMEA sensor after casting, c) placement of ER sensors and steel reinforcing bars before casting, and d) specimen with ER sensor and steel reinforcing bars after casting. The figure illustrates the geometry and scale of the test specimens used for corrosion monitoring.

Table 2
Chemical composition* of the various carbon steels used in this study.

Steel type	Used for	C* [wt%]	P* [wt%]	S* [wt%]	Cu* [wt%]	N* [wt%]	C_{eq}* [wt%]
Reinforcing bar Φ14 mm	Visual analysis	0.15	0.020	0.043	0.40	0.013	0.33
Reinforcing bar Φ6 mm	Visual analysis	0.13	0.019	0.016	0.09	-	-
Steel sheet	ER sensor	0.07	0.011	0.013	0.10	0.009	0.14
Steel wire Φ0.5 mm	CMEA sensor	0.87	0.041	0.009	0.02	-	-

* *According to the EN 10080:2005 standard for weldable reinforcing steel in concrete, the maximum allowable content [wt%] for individual elements is* $C \leq 0.24$, $S \leq 0.055$, $P \leq 0.055$, $N \leq 0.014$, *and* $Cu \leq 0.85$. *The carbon equivalent* (C_{eq}), *which is limited to* $C_{eq} \leq 0.52$, *is calculated using the formula:* $C_{eq} = C + Mn/6 + (Cr + Mo + V)/5 + (Ni + Cu)/15$.

2.3. Techniques

This section describes the operation of two unconventional methods for monitoring corrosion, specifically CMEA and ER sensors, which were used along with microCT visual assessment.

The CMEA sensor effectively simulates a larger steel surface by combining multiple steel electrodes into a coupled electrode array. The coupling currents between individual electrically connected electrodes can then be measured. This configuration allows monitoring of the spatiotemporal corrosion pattern, including the distribution of anodic and cathodic currents over time. Each coupling current is measured using a zero-resistance ammeter (ZRA), ensuring that all sections of the specimen maintain the same electrical potential, with no external potentials or currents being imposed.

The use of an ER sensor represents a physical corrosion monitoring technique. These sensors are made of a steel sheet etched into a long and thin steel conductor shaped as a Wheatstone bridge, where two resistors are exposed to corrosion, and two resistors are protected and act as reference resistors. The Wheatstone bridge design is used to compensate the temperature, as well as any fluctuations in the electrical current. The working principle of the ER sensor is to measure the increase in electrical resistance as the cross-section is reduced due to corrosion [27]. The measured change in resistance can be converted directly into the average thickness reduction and the average corrosion rate across both exposed electrodes. More details on the calculation of thickness reduction and corrosion rates can be found in our previous study [43].

2.4. Specimens and exposure

For each of the three AAMs studied, three types of specimen were constructed (Fig. 1). The dimensions and geometries of these specimens were tailored to accommodate the characteristics of the corrosion tests, including the incorporation of embedded steel electrodes and/ or corrosion sensors. After casting, all mortar specimens were cured within sealed plastic foil for a period of 28 days. After curing, all specimens were exposed to alternating wet and dry cycles—initially in a 3.5 % NaCl solution for 10 weeks, then later transitioning to deionized water due to the accumulation of chloride on the specimen surface. This adjustment aimed to avoid extensive increases in surface chloride concentration and to allow more realistic chloride redistribution into the mortar during subsequent wetting and drying cycles.

2.4.1. Coupled multi-electrode array (CMEA) sensors

The first type of specimen was equipped with coupled multi-electrode array (CMEA) sensors (Chapter 2.3. Techniques), as illustrated in Fig. 1a. In this study, the CMEA sensor was constructed using 25 carbon steel wire electrodes (Chapter 2.2. Properties of the steels), each having a diameter of 0.50 mm and a nominal individual electrode surface area of 0.196 mm^2 (resulting in an overall surface area of 4.9 mm^2 for 25 electrodes). The minimum distance between the electrodes was 0.5 mm (center-to-center distance of 1 mm). These electrodes were organized in a grid of 5 by 5 and encapsulated within epoxy resin. Before casting in mortar, the CMEA sensors were abraded using P1200 grit emery paper, followed by ultrasonic cleaning in ethanol and subsequent drying to remove fine particles and grease from the exposed electrodes. The AAM cover above the CMEA sensor was 10 mm thick. Each week, the specimens were wetted with 1 mL NaCl solution (or deionized water) from the pool atop each specimen, which evaporated in approximately 24 h, allowing the specimens to dry for approximately 6 days in each cycle. Measurements spanned several weeks, i.e., 22–37 wet/ dry cycles, with most conducted over 30 weeks. The CMEA measurements were conducted using a custom-designed zero resistance ammeter which utilized resistors and power supplies capable of detecting a maximum current (I) of 250 μA. Measurements of the coupled currents were continuous, while the data acquisition frequency was set at 1 Hz. Prior to connecting each specimen, the internal device offsets for each ammeter were determined and set to zero. The currents measured were presented as current densities (j), i.e., the amount of current flowing per unit area of the electrode's surface.

The *real-time current densities* (j_{RT}) were graphically presented as the real-time anodic (j_{corr}) and cathodic (j_{cath}) current densities measured at a specific moment during the corrosion process. The *anodic current densities* (j_{corr}) represent the positive values of j_{RT} measured and can also be referred to as the *corrosion current density* as they are directly associated with corrosion damage. The *cathodic current densities* (j_{cath}) represent the negative values of j_{RT} measured. The *real-time corrosion rates* (ν_{corr}) were calculated from the anodic (corrosion) current densities (j_{corr}) according to Eq. 1 [44], using an atomic mass of steel (*AM*) of 55.1 g, a Faraday constant of $F = 9.65 \times 10^4$ As, a valence of $n = 2$, and a steel density of $\rho = 7.85$ g/cm^3.

$$\nu_{corr} = \frac{AM \bullet j_{corr}}{n \bullet F \bullet \rho} \tag{1}$$

The *average (local) anodic current density* ($j_{corr\text{-}AVERAGE}$), also referred to as the *average (local) corrosion current density*, is calculated from the j_{corr} values measured on individual electrodes over the selected exposure time according to Eq. 2, where t_{total} represents the total time for the interval being calculated, Δt_i is the time interval between the measurements i and i − 1, and m is the number of measurements. The *maximum average anodic current density* ($j_{corr\text{-}AVERAGE\text{-}max}$) is the average current density on the most anodic electrode over the selected exposure time.

$$j_{corr-AVERAGE} = \frac{1}{t_{total}} \sum_{i=1}^{m} \Delta t_i j_{corr-i} \tag{2}$$

The *average corrosion rate* ($\nu_{corr\text{-}AVERAGE}$) is derived from $j_{corr\text{-}AVERAGE}$ according to Eq. 1 (using$\nu_{corr\text{-}AVERAGE}$ instead of ν_{corr} and $j_{corr\text{-}AVERAGE}$ instead of j_{corr}). The *average cathodic current density* ($j_{cath\text{-}AVERAGE}$) is calculated from the j_{cath} measured on each individual electrode over the entire period of exposure.

The *general anodic (corrosion) current density* ($j_{corr\text{-}GENERAL}$) is the $j_{corr\text{-}AVERAGE}$ averaged across all of the electrodes over the selected exposure time using Eq. 3, where n represents the number of electrodes (in this case $n = 25$); the *general corrosion rate* ($\nu_{corr\text{-}GENERAL}$) is derived from $j_{corr\text{-}GENERAL}$ using Eq. 1 (using$\nu_{corr\text{-}GENERAL}$ instead of ν_{corr} and $j_{corr\text{-}GENERAL}$ instead of j_{corr}) and indicates the general corrosion rate over the entire surface of the CMEA sensor (all electrodes), producing a result comparable to those obtained from the electrochemical techniques usually used.

$$j_{corr-GENERAL} = \frac{1}{n} \sum_{i=1}^{n} j_{corr-AVERAGE-i} \tag{3}$$

The *total corrosion damage depth (D)* was calculated by integrating the corrosion rate (ν_{corr}) over a period of time according to Eq. 4, or, in the case of the constant corrosion rate (ν_{corr}), according to Eq. 5, where t_0 is the starting time of the exposure and $D(t)$ is the total corrosion damage at the selected time, t.

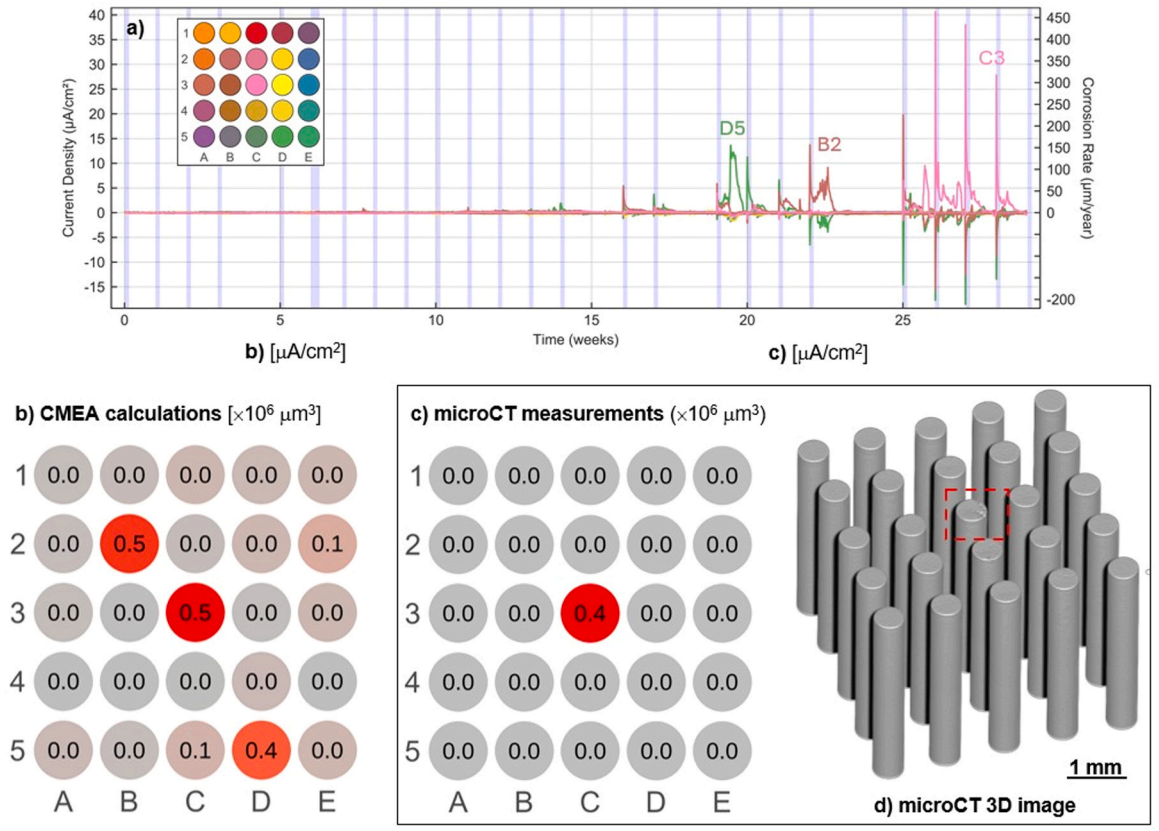

Fig. 2. A CMEA sensor embedded in the FA8 (fly ash) alkali-activated mortar: a) continuous measurements of the ANODIC (positive, j_{corr}) and CATHODIC (negative, j_{cath}) current densities (grey sections = wetting, white sections = drying), b) corrosion damage calculated from the CMEA anodic currents (D_V) measured, c) corrosion damage measured from the microCT scans, and d) a microCT 3D image of the CMEA following the period of exposure.

$$D(t) = \int_{t_0}^{t} \nu_{corr}(\tau) d\tau \tag{4}$$

$$D(t) = \nu_{corr}(t - t_0) \tag{5}$$

The spatial resolution of CMEA is determined by the electrode cross-section (lateral) and the accuracy of the ZRA device (depth). Assuming uniform corrosion across the electrode surface, the depth resolution can be estimated using Faraday's law of electrolysis.

The *total corrosion damage volume (D_V)* was calculated using Eq. 6. A simplified cylindrical geometry of the corrosion damage was assumed, where $S = 0.196$ mm^2 is the surface of one electrode and D is the total corrosion damage depth."

$$D_V = D \bullet S \tag{6}$$

Visual analysis of the CMEA sensors embedded in the AAMs was performed before and after the exposure to wet/ dry cycles using X-ray computed microtomography (microCT). The scanning was conducted with a Zeiss Xradia microCT-400 device (Xradia, 2012) covered by a HE#1 proprietary filter, using a source voltage of 150 kV, a power of 10 W, and a CCD detector with a macro lens. The scanning settings were as follows: 8 s exposure time per image, 1601 images per scan, and 1 scan per specimen, resulting in a voxel resolution of 9 μm. The microCT data were processed using Avizo Inspect (FEI) and Dragonfly 3D World (Comet/ORS) software. Avizo was used to segment the greyscale images in binary images, while Dragonfly was used to subtract and quantify the total corrosion damage volume (D_V), and to visualize the corrosion damage (e.g., Fig. 2). The following detailed procedure was employed to determine the corrosion damage volumes from the CT scans: Initially, the scans of both the undamaged CMEA specimen (before exposure) and the damaged CMEA specimen (after exposure) were interactively thresholded using Avizo to segment the metal electrodes from the rest of the specimen. Once the threshold value for the first specimen was determined, the same value was used for the other specimens, as the reconstructed greyscale images were normalized beforehand using Zeiss own reconstruction software. The binary images resulting from the thresholding were exported to Dragonfly. After segmentation, the undamaged electrodes were converted into multi-ROIs (regions of interest) using Dragonflies built-in tool, with each electrode treated as a separate entity. Subsequently, the segmented metal portion of the damaged CMEA specimen was subtracted from the non-damaged separated multi-ROI electrodes using binary subtraction tool, which isolated the volume of electrodes that had corroded over time (D_V). The damaged volumes for each electrode were exported as CSV files.

2.4.2. Electrical resistance (ER) sensors and steel reinforcing bars

The second set of specimens (Fig. 1b), with dimensions of 360 × 135 × 40 mm, were equipped with electrical resistance (ER) sensors [27] (Chapter 2.3. Techniques) and two B 500B steel reinforcing bars with diameters of Φ6 mm and Φ14 mm (Chapter 2.2. Properties of the steels). The steel reinforcing bars were only used for visual assessment purposes. The specimens with embedded ER sensors and reinforcing steel bars were wetted with 100 mL of 3.5 % NaCl solution (or deionized water) from the pool atop each specimen and dried after 1 day, allowing the specimens to dry for approximately 6 days in each cycle. Each measurement protocol lasted several weeks, *i.e.,* between 8 and 66 wet/ dry cycles. The measurements were performed both automatically and manually. The automatic measurements were continuous, providing a larger amount of data (1 measurement every 10 min), while the manual measurements were more discrete, with fewer data points collected over the course of the exposure (approximately 1 measurement each week). The electrical resistance of the ER sensors, and consequently their thicknesses, were measured either automatically (continuously, with 1 measurement every 10 min) or manually (approximately 1 measurement each week, conducted immediately after wetting the specimens).

Visual imaging of the ER sensors embedded in the AAMs was performed at the end of the exposure to wet/ dry cycles using X-ray computed microtomography (microCT). The scanning was carried out using a Zeiss Xradia microCT-400 device (Xradia, 2012) with the voxel resolution set at 30 μm. The other recording parameters were the same as those used for the CMEA scanning: 150 kV source voltage, 10 W power, 8 s exposure time per image, 1601 images per scan, and 1 scan per specimen. The microCT data were processed using Avizo Inspect (FEI).

Following the end of the exposure, the corrosion products and any mortar fragments adhered to the steel bars embedded in the mortar specimens were dissolved with a solution composed of concentrated HCl mixed with deionized water at a ratio of 50:50 (vol%) with 3 g/L $C_6H_{12}N_4$ (hexamethylenetetramine). Subsequently, the corrosion damage on the steel bars was examined through visual inspection. Visual analysis was employed as a supplementary method to validate the findings from the corrosion measurements, aiding in the identification and assessment of the type and severity of corrosion.

3. Results

3.1. Coupled multi-electrode array (CMEA) sensors

The first type of specimen was equipped with a coupled multi-electrode array (CMEA) sensor for monitoring the spatiotemporal distribution of anodic and cathodic currents on 25 carbon steel wire electrodes in three types of AAM, based on fly ash (FA8), metakaolin (MK2), or slag (S3a-661). The total exposure time was between 22 and 37 weeks (30 weeks for the majority of specimens).

3.1.1. CMEA measurements in fly ash-based AAM

Two parallel samples with CMEA sensors installed in the FA8 (fly ash-based) mortar showed very comparable results (Fig. 2 and

Supplementary Fig. 1). The anodic and cathodic currents, which were continuously measured on each individual electrode over 28 weeks (cycles) of exposure, are presented in Fig. 2a as the real-time current densities (j_{RT}) and real-time corrosion rates (ν_{corr}) calculated from the real-time anodic (corrosion) current densities (j_{corr}). Corrosion was observed on only 3 electrodes, indicating localized corrosion (Fig. 2b). In both measurements, the average corrosion current densities ($j_{corr\text{-}AVERAGE}$) were found to be low (up to 0.4 μA/cm^2; electrodes B2 and C3, Fig. 2), corresponding to an average corrosion rate ($\nu_{corr\text{-}AVERAGE}$) of 4.6 μm/year. The initial (constant) deviations towards anodic behavior (indicating the initiation of corrosion) were recorded in cycle 11 (up to 6 μA/cm^2), with larger deviations starting in cycle 20 (up to 15 μA/cm^2, Fig. 2a) and cycle 26 (up to 40 μA/cm^2). The cathodic sites with very low average cathodic current densities ($j_{cath\text{-}AVERAGE}$) were fairly evenly distributed across all of the electrodes (Fig. 2c). Therefore, very low but local anodic processes and more general cathodic processes were measured in this FA8 mortar. Furthermore, no anode electrode remained solely anodic throughout the entire exposure period—all electrodes transitioned to the cathodic region at some point. This pattern is especially noticeable in the last three weeks of exposure (W27-W29), where the electrodes (B2, D5) with the highest average corrosion current densities ($j_{corr\text{-}AVERAGE}$) simultaneously exhibited the most negative average cathodic current densities ($j_{cath\text{-}AVERAGE}$; Fig. 3). This suggests that there is easy access to oxygen and other reactants during the final stages of exposure, most likely due to the formation of microcracks in the mortar cover.

A comparison of the corrosion damage calculated from the CMEA currents with the corrosion damage measured by microCT showed good agreement for one measurement (Supplementary Fig. 1b-d), while the anodic currents from the second measurement (Fig. 2b-d) do not entirely correspond with the microCT analysis for two of the electrodes (B2 and D5). It should be considered that the corrosion currents measured were very low, as was the corrosion damage measured with microCT. Any visible damaged features in the two electrodes (B2 and D5) were lower than 3-times the microCT scanning resolution, which is generally considered the cutoff size for accurate quantification of the results. In the case that corrosion damage occurs equally across the exposed electrode surface, the changes will likely not be visible at the microCT resolution given.

3.1.2. CMEA measurements in metakaolin-based AA

A CMEA sensor was also installed in two parallel specimens of the MK2 (metakaolin-based) mortar, showing comparable results for

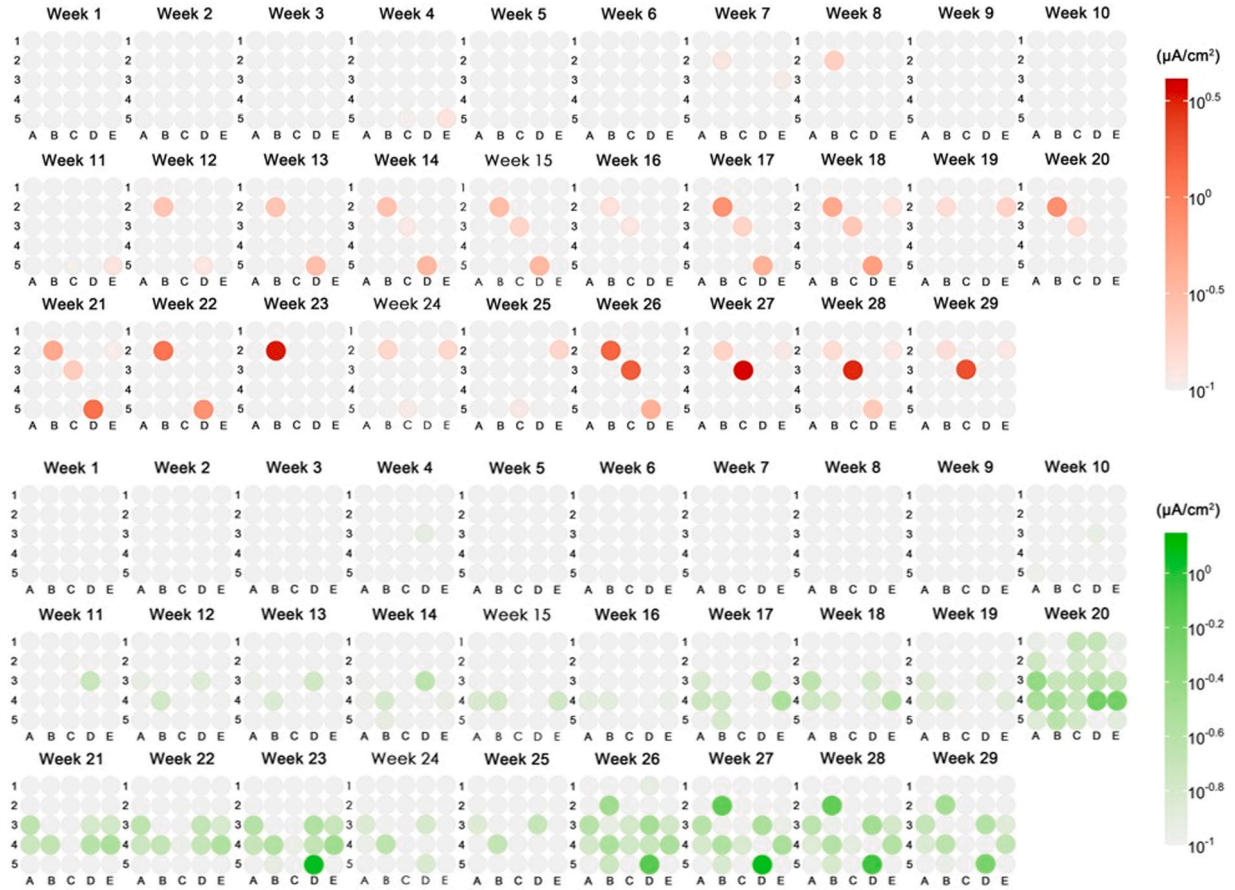

Fig. 3. A CMEA sensor embedded in the FA8 (fly ash) alkali-activated mortar: the average anodic current densities ($j_{corr\text{-}AVERAGE}$, red) and average cathodic current densities ($j_{cath\text{-}AVERAGE}$) measured on individual electrodes over each one week cycle throughout the period of exposure. The scale was set to a minimum of 0.1 μA/cm^2, reflecting the widely accepted threshold for corrosion initiation in steel embedded in concrete [45,46].

both measurements (Fig. 4, Supplementary Fig. 2). Localized corrosion was observed, but it occurred on more electrodes (6) than in the FA8 specimens (Fig. 4b). The average anodic (corrosion) current densities ($j_{corr\text{-}AVERAGE}$) over the entire exposure period was found to be low, reaching a maximum of 4.1 μA/cm^2 (electrode C4). The corresponding maximum $\nu_{corr\text{-}AVERAGE}$ of 47 μm/year is higher than that measured in the FA8 mortar. Deviations towards anodic behavior (indicating the initiation of corrosion) were measured in the seventh wetting cycle (values of up to 9 μA/cm^2, Fig. 4a). Larger, very local deviations (up to 50 μA/cm^2) started in cycle twelve, mostly on electrode B2. Towards the end of the exposure (cycles 26–29, up to 150 μA/cm^2) the corrosion behavior represents a combination of localized and uniform corrosion, with the anodic activity beginning on one electrode and then spreading to the neighboring electrodes over the following weeks, while the initially active electrode remains anodic for an additional week or two. Unlike in the FA8 specimen, all of the electrodes were cathodic at least at some point during the exposure, as the lowest $j_{cath\text{-}AVERAGE}$ is 0.1 μA/cm^2, while the most negative $j_{cath\text{-}AVERAGE}$ values were very localized on several individual electrodes, namely A4, B4, and B2 (Fig. 4c). Although cathodic processes were also measured on most of the anodic electrodes (Fig. 5), up until Week 26 of the exposure the highest $j_{cath\text{-}AVERAGE}$ values are measured on different electrodes than those exhibiting the highest $j_{corr\text{-}AVERAGE}$. The most anodic electrode from Week 13 (B2) slowly fades and becomes the most cathodic electrode in Week 26. It could be assumed that, during anodic periods, voluminous corrosion products were formed, thus changing the steel-mortar interface (e.g. the development of cracks or crevices) and enabling access to oxygen.

A comparison of the corrosion damage calculated from the CMEA currents with the corrosion damage measured by microCT (Fig. 4b-d, Supplementary Fig. 2b-d) shows very good agreement in both measurements. The absence of high anodic currents until Week 26 (Fig. 5) on some of the most corroded electrodes C4 and C5 (Fig. 4d) suggests that the most severe corrosion damage on these electrodes occurred only during the last three weeks of exposure. The damage observed on the B2 electrode, however, is the result of longer term (W8-W26) anodic processes on this electrode.

3.1.3. CMEA measurements in slag-based AAM

Measurements on the CMEA sensors installed in two parallel specimens made of S3a-661 (slag-based) mortar were comparable in terms of the corrosion location and the current density values (Fig. 6, Supplementary Fig. 3). In both measurements, localized average anodic currents were observed, with 5 electrodes having a higher average anodic current density ($j_{corr\text{-}AVERAGE}$), similar to that seen in

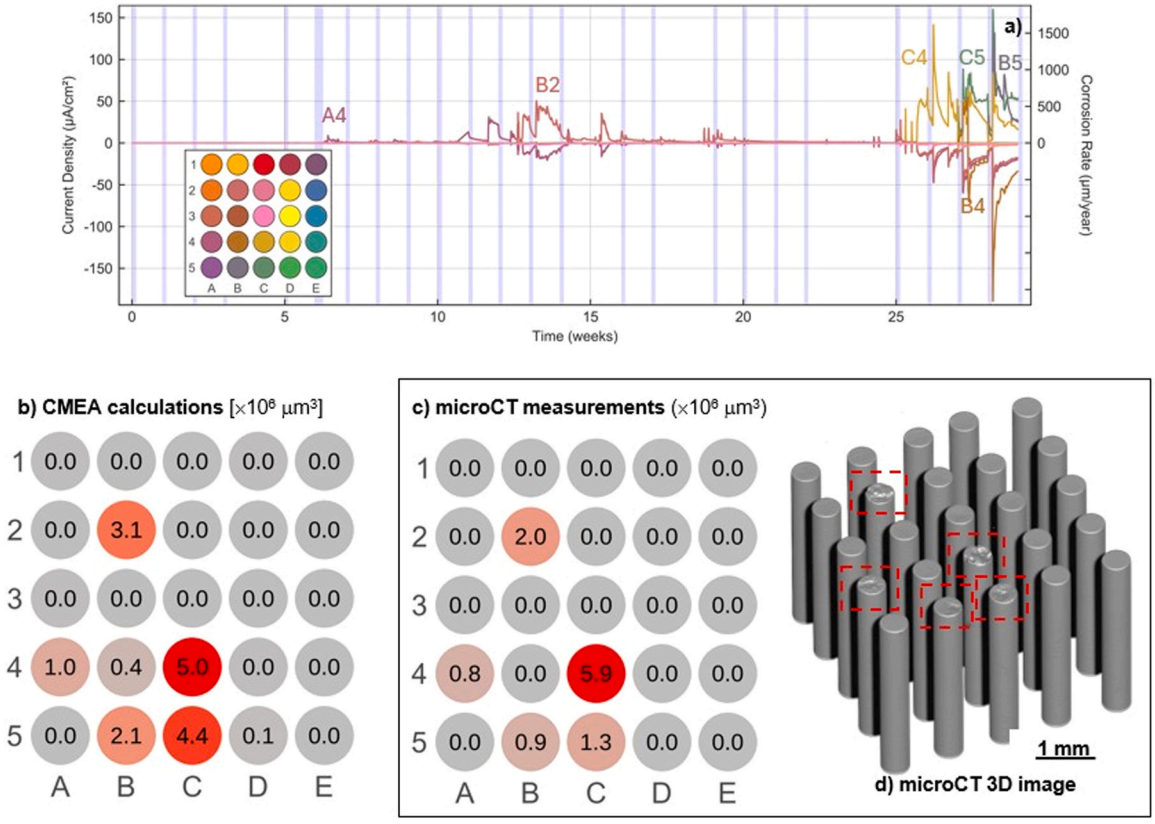

Fig. 4. A CMEA sensor embedded in the MK2 (metakaolin) alkali-activated mortar: a) continuous measurements of the ANODIC (positive, j_{corr}) and CATHODIC (negative, j_{cath}) current densities (grey sections = wetting, white sections = drying), b) corrosion damage calculated from the CMEA anodic currents (D_V) measured, c) corrosion damage measured from the microCT scans, and d) a microCT 3D image of the CMEA following the period of exposure.

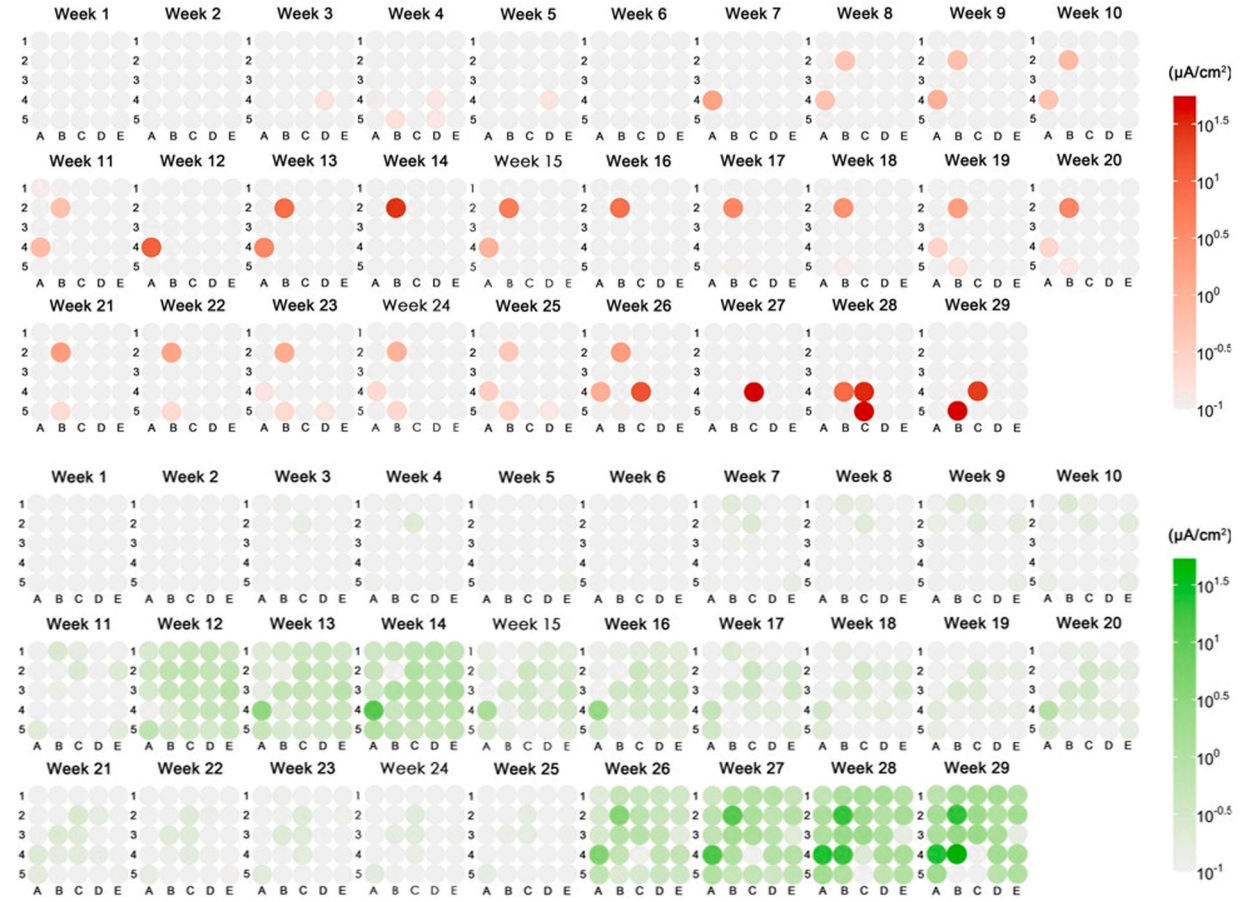

Fig. 5. A CMEA sensor embedded in the MK2 (metakaolin) alkali-activated mortar: average anodic current densities ($j_{corr\text{-}AVERAGE}$, red) and average cathodic current densities ($j_{cath\text{-}AVERAGE}$) measured on individual electrodes over each one week cycle throughout the period of exposure. The scale was set to a minimum of 0.1 μA/cm^2, reflecting the widely accepted threshold for corrosion initiation in steel embedded in concrete [45,46].

the MK2 specimens (Fig. 6). The average anodic current densities ($j_{corr\text{-}AVERAGE}$) measured throughout the entire period of exposure were low, being comparable to those of the MK2 specimens, with values of up to 4.0 μA/cm^2 (some $j_{corr\text{-}AVERAGE}$ values in Supplementary Fig. 3 were slightly higher due to slight crevice corrosion), corresponding to a maximum $\nu_{corr\text{-}AVEARGE}$ of 46 μm/year. In both measurements, initial deviations towards anodic behavior (up to 15 μA/cm^2, indicating the initiation of corrosion) were recorded as early as cycle 1, with similar levels then shown in each subsequent cycle. Larger deviations began after cycle 12, with higher deviations of up to 100 μA/cm^2. Cathodic sites were distributed across all the electrodes, with individual electrodes showing slightly more negative average cathodic current densities ($j_{cath\text{-}AVERAGE}$), as shown in Fig. 6c. At the beginning of the exposure (Fig. 7), the most negative $j_{cath\text{-}AVERAGE}$ values were typically measured on the same as those exhibiting the highest $j_{corr\text{-}AVERAGE}$ or on their neighboring electrodes. The most anodic electrode from Week 1 (A1) gradually becomes the most cathodic electrode (as with B2 in the MK2 mortar), while electrodes C3, B2, and B5 change between anodic and cathodic behavior throughout the exposure.

A comparison of the corrosion damage calculated from the CMEA currents (volume in μm^3) with the corrosion damage measured by microCT (Fig. 6b-d) showed good agreement in certain locations. However, on the electrodes with crevice corrosion, shown in Supplementary Fig. 3b-d, the numerical values of the actual damage observed by microCT were higher than those measured from the CMEA currents.

3.2. *Electrical resistance (ER) sensors and steel reinforcing bars*

The second set of specimens were equipped with electrical resistance (ER) sensors, with the reduction in their cross-section measured to reflect the extent of corrosion (Fig. 8). Two B 500B steel reinforcing bars with diameters of Φ6 mm and Φ14 mm were embedded in the same specimens merely for the purpose of visual assessment.

The results of the measurements from the ER sensors show that the best corrosion performance was exhibited by the steel in the S3a-661 (slag-based) mortar—one of the ER sensors showed no loss in thickness during its 66 weeks of exposure to wet/ dry conditions, while the other one only started to corrode towards the end of the exposure, when it experienced an instant loss in thickness after 4

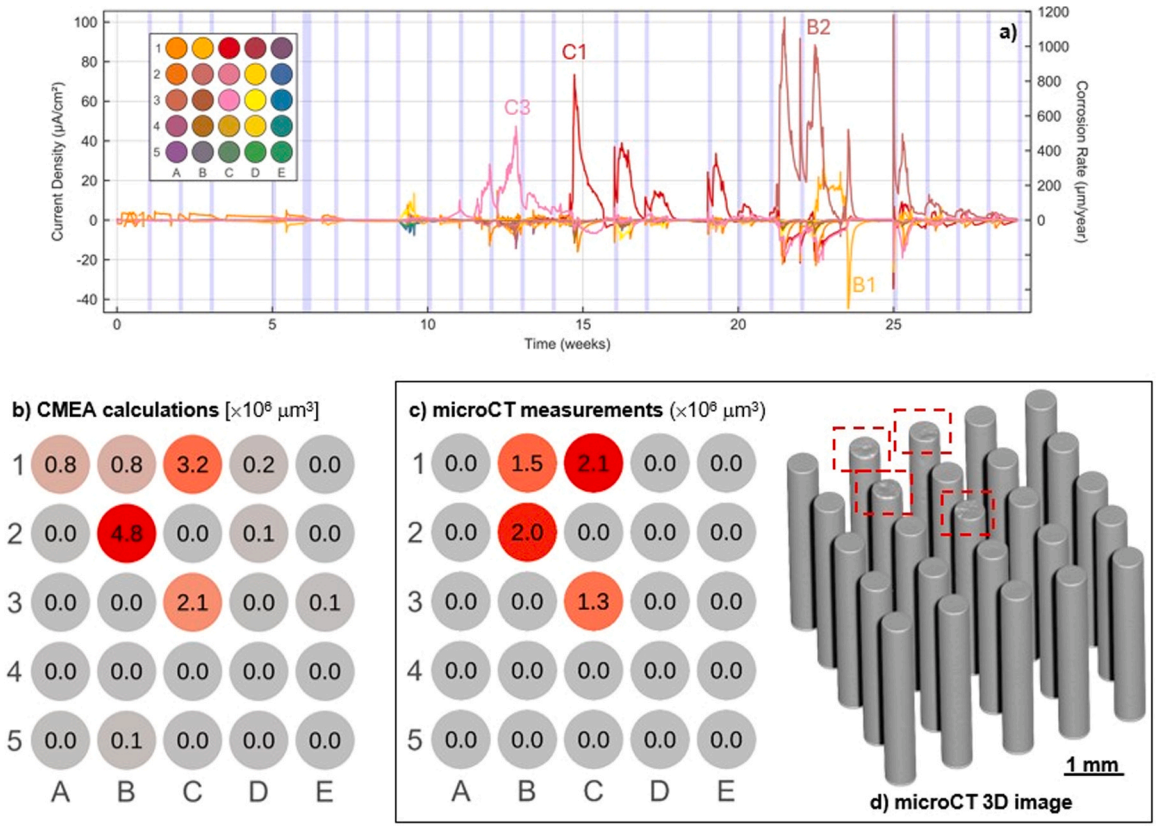

Fig. 6. A CMEA sensor embedded in S3a-661 (slag) alkali-activated mortar: a) continuous measurements of the ANODIC (positive, j_{corr}) and CATHODIC (negative, j_{cath}) current densities (grey sections = wetting, white sections = drying), b) corrosion damage calculated from the CMEA anodic currents (D_V), c) corrosion damage measured from the microCT scans, and d) a microCT 3D image of the CMEA following the period of exposure.

weeks of mild thinning (Fig. 8a). This result is supported by the microCT image, which shows no visible damage on the first ER sensor and only very local corrosion damage on the second sensor (Fig. 8b). To a certain extent, the ER sensor measurements align with the actual damage to the reinforcement (Fig. 8c). However, the reinforcement exhibits more severe corrosion damage than that observed on the ER sensors, with dense pitting and some areas showing a significant depth of damage. This discrepancy indicates that the ER sensor and reinforcement might be exhibiting different corrosion rates, which could be influenced by differences in the steel properties [47,48].

The most aggressive corrosive environment for the ER sensor was in the MK2 (metakaolin-based) mortar. Rapid thinning was observed on both of the ER sensors (Fig. 8a), with them becoming completely corroded in either 9 or 20 weeks, indicating the extremely localized corrosion damage. MicroCT imaging (Fig. 8b) confirmed this finding, revealing severe corrosion damage at multiple points on the sensor, appearing as pitting corrosion. This extensive sensor damage corresponds to the condition of the reinforcement bars (Fig. 8c), where the local corrosion damage is deep and sparsely distributed. Additionally, a reduction in the bar diameter was measured, indicating general corrosion around the locally damaged areas.

The thinning of the ER sensors measured in the FA8 (fly ash-based) mortar was uniform up to Week 62 or 35, after which a sudden drop in thickness was measured (Fig. 8a). This sudden change aligns well with observations of the microCT images of the ER sensors (Fig. 8b), which show damage across the entire surface, but also show more severe localized corrosion damage. The actual damage to the reinforcement can be well correlated with the ER sensor measurements, which show a mixed pattern of corrosion damage (Fig. 8c). Some regions exhibit isolated patches of minor local corrosion, while others showing more general corrosion.

4. Discussion

4.1. Coupled multi-electrode array (CMEA) sensors

A comparative analysis of the CMEA measurements in the FA8, MK2, and S3a-661 mortars confirmed the capability of this technique to monitor corrosion behavior and its dynamic electrochemical activity, including corrosion initiation, propagation, and current distribution (Fig. 2a, Fig. 4a, and Fig. 6a). MicroCT scans of the CMEA sensors confirmed good spatial agreement with the

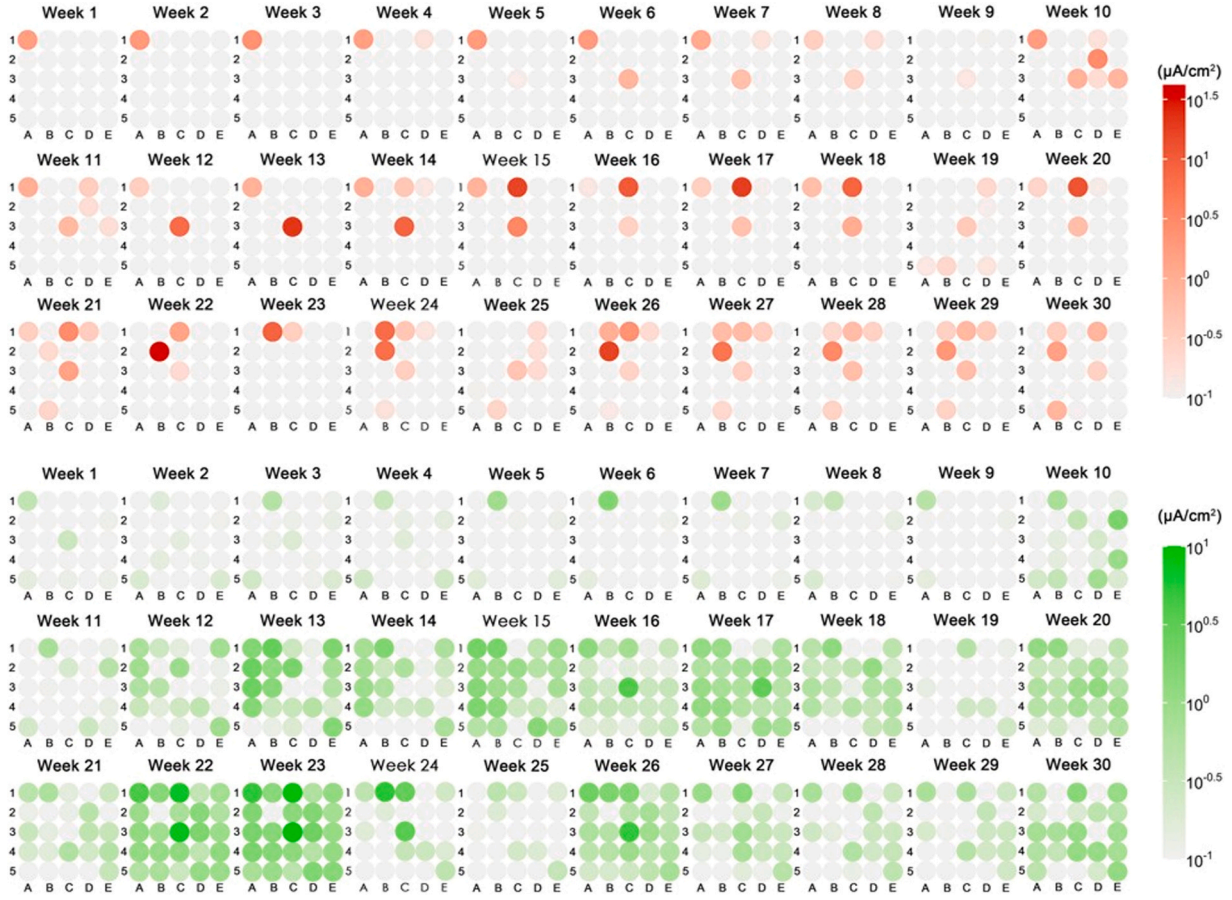

Fig. 7. A CMEA sensor embedded in S3a-661 (slag) alkali-activated mortar: the average anodic current densities ($j_{corr\text{-}AVERAGE}$, red) and average cathodic current densities ($j_{cath\text{-}AVERAGE}$) measured on individual electrodes over each one week cycle of the period of exposure. The scale was set to a minimum of 0.1 μA/cm², reflecting the widely accepted threshold for corrosion initiation in steel embedded in concrete [45,46].

estimated corrosion damage (Fig. 2b-d, Fig. 4b-d, and Fig. 6b-d). Certain discrepancies noted at low damage levels probably originated from the microCT resolution.

When using conventional electrochemical techniques, specific parameters (e.g., current, polarization resistance) are typically estimated over the entire surface of the working electrode. A similar methodology can be applied to CMEA measurements to enable comparison with other techniques. Fig. 9a shows the general anodic (corrosion) current densities ($j_{corr\text{-}GENERAL}$) calculated for each week of exposure, where the total anodic current was divided by the total surface area of all 25 electrodes. It can be seen that the general current densities in MK2 and S3a-661 mortars increased after week 10. Thereafter, the general current density in S3a-661 mortar remained relatively stable, but showed distinct fluctuations. (i.e., large variations between weekly values). In contrast, the average current density in MK2 mortar increased significantly after week 25. The lowest general current density was observed in the FA8 mortar, although a continuous increase over time was observed.

The highest local corrosion rates for each week were obtained by identifying the most anodic electrode during that week ($j_{corr\text{-}AVERAGE\text{-}max}$) and calculating its corrosion rate (Fig. 9b). Localized corrosion rates were approximately one order of magnitude higher than the general rates. While the overall trends remained mostly similar, fluctuations in localized rates were particularly noticeable in the S3a-661 mortar.

To assess the localization of the corrosion processes from the CMEA measurements, the corrosion localization index (CLI, Eq. 7) was introduced [35]. This is defined as the ratio of the maximum average anodic current density ($j_{corr\text{-}AVERAGE\text{-}max}$) to the general anodic (corrosion) current density ($j_{corr\text{-}GENERAL}$). An index value of 1 indicates uniform distribution of general corrosion across all of the electrodes, while a ratio of 25 signifies highly localized corrosion, where only one electrode corroded. The distribution of CLI values in the individual AAMs throughout the whole period of exposure is presented in Table 3.

$$CLI = \frac{j_{corr-AVEARGE-\max}}{j_{corr-GENERAL}} \tag{7}$$

The estimated CLI showed more general corrosion for FA8 mortar compared to MK2 and S3a-661 (up to 13), becoming more local only in the last 3 weeks of exposure (CLI 19). The CMEA sensor in MK2 mortar experienced rather local corrosion (a CLI of up to 23.4)

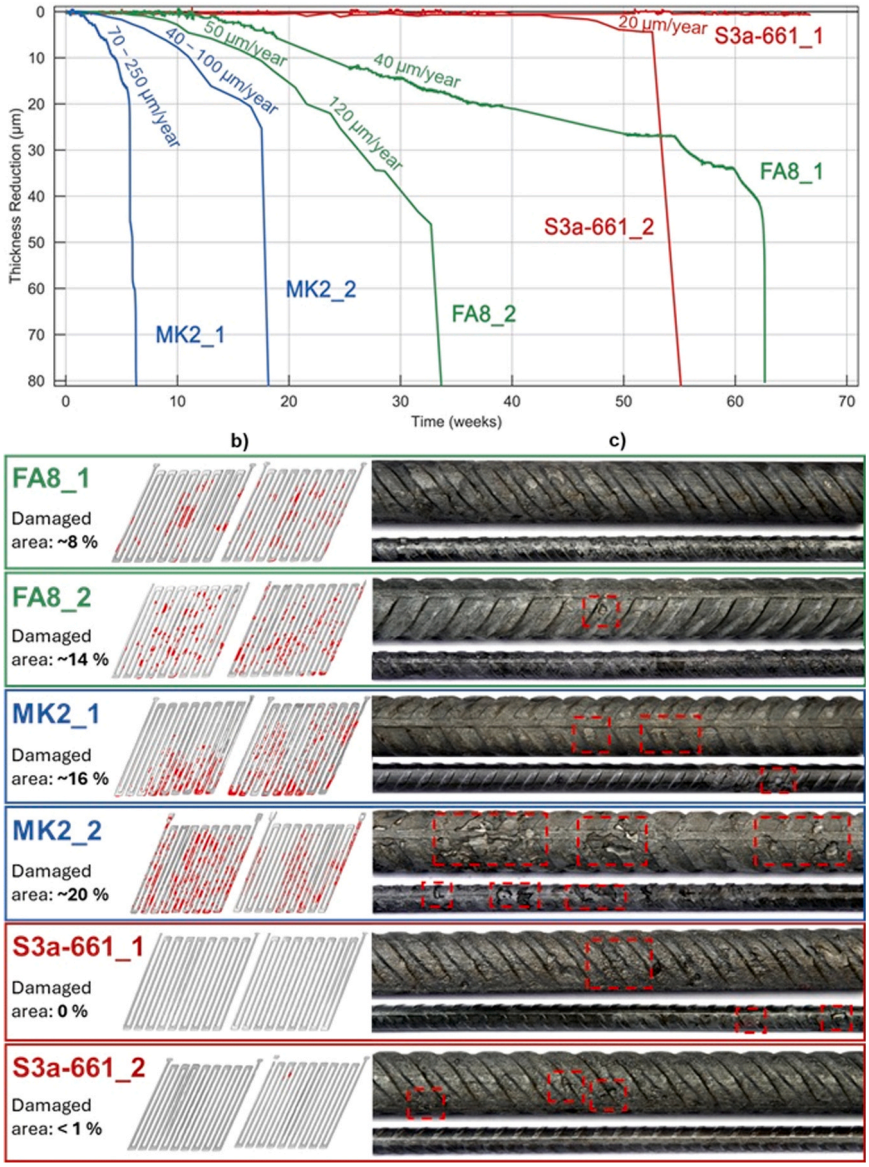

Fig. 8. a) Thickness reduction of the ER sensors embedded in different AAMs, b) microCT scans of the corresponding ER sensors with the red regions indicating perforating corrosion, and c) steel bars embedded in the same AAM specimens (the parts with the most severe typical damage are presented).

in the earlier period but became more general toward the end of the exposure (CLI 12). The most localized corrosion, both at the beginning and later in the exposure period, was observed in the S3a-661 mortar (CLI 20.6). However, indications of more general corrosion also appeared over time (CLI 13–14), as shown in Table 3.

The observed fluctuations in corrosion current densities, particularly in the later stages of exposure (Figs. 2a, 4a and 6a), are attributed to changes in oxygen availability and conductivity during wet–dry cycles, further intensified by the progressive accumulation of chlorides [26,27]. In all of the mortars the anodic current was limited to a few electrodes, while the cathodic current was more widely distributed across the electrodes. A common feature is also the dynamic nature of the anodic activity—an electrode may act as an anode for several cycles before its activity diminishes or even shifts to cathodic behavior, while another electrode becomes anodic. Initially, these anodic shifts occurred over periods of 5–10 weeks, but the transitions accelerated over time. With a longer exposure, these transitions are expected to occur more rapidly, what may finally lead to fairly general corrosion damage across all of the electrodes. These transitions between anodic and cathodic states were observed in all three mortars, particularly during the later stages of exposure. This suggests that the passive film on the electrodes deteriorated, while cracks formed (whether due to corrosion products or mortar degradation), thus accelerating the transport processes.

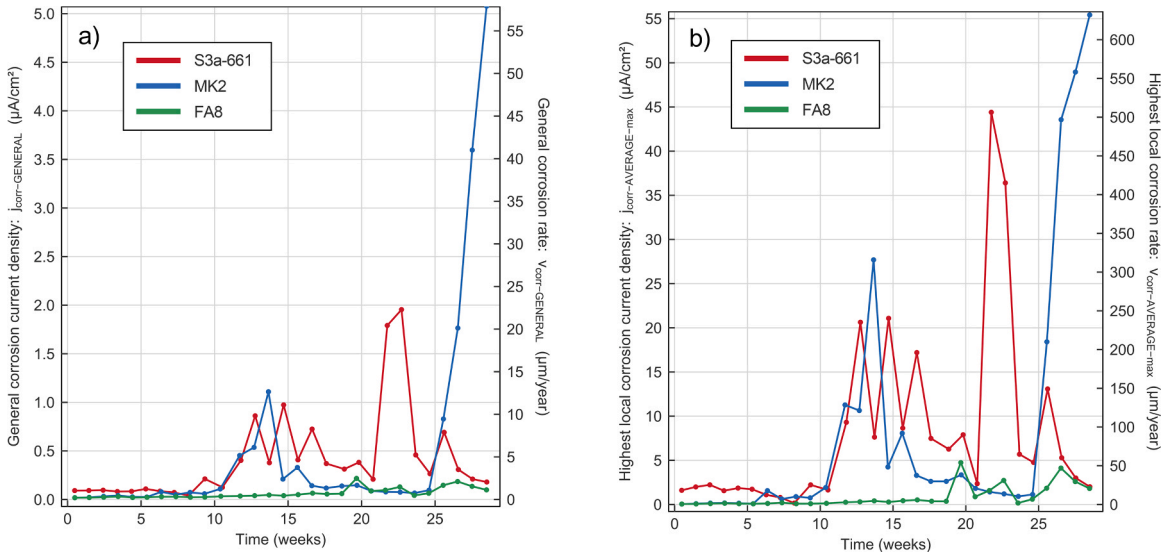

Fig. 9. a) General corrosion (anodic) current densities ($j_{corr\text{-}GENERAL}$) and calculated general corrosion rates ($\nu_{corr\text{-}GENERAL}$) across all 25 electrodes, averaged for each week; (b) the highest local (anodic) current densities ($j_{corr\text{-}AVERAGE\text{-}max}$) and calculated highest local corrosion rates ($\nu_{corr\text{-}AVERAGE\text{-}max}$), averaged for each week.

Table 3
Corrosion Localization Index (CLI) distribution at 3-week intervals over the entire exposure period.

	W1-W3	W4-W6	W7-W9	W10-W12	W13-W15	W16-W18	W19-W21	W22-W24	W25-W27	W28-W29
FA8	3.35	3.96	4.81	4.84	7.47	7.41	12.7	12.9	12.2	19.3
MK2	3.74	4.14	14.8	15.4	20.9	23.4	20.5	16.2	17.5	12.2
S3a-661	20.6	18.7	7.57	14.2	21.4	22.2	13.6	18.7	14.3	12.9

4.2. Electrical resistance (ER) sensors and steel reinforcing bars

The results confirmed the use of ER sensors as an effective method for corrosion monitoring also in AAM mortars. The sensors reliably detected corrosion initiation and assessed the general corrosion rate. It was revealed that the typical exponential behavior of the corrosion rate over time indicates the growth of one or more pits [49]. Although, in this sense, differentiation between general and localized corrosion can be made, this is not possible until the ER sensor undergoes a significant reduction in its cross-section.

It is evident that the corrosion rate of one of the sensors in the FA8 mortar (FA8_1) was fairly constant, while this was not entirely true for the FA8_2 sensor (Fig. 8a). It can therefore be concluded that the corrosion of FA8_1 was predominantly general, whereas with FA8_2 localized corrosion was also present. The corrosion rate in the MK2 mortar increased exponentially in both ER sensors, and a significant shift appeared just after either 9 or 19 weeks after the start of the exposure (Fig. 8a). Such responses in the ER sensors indicated intense localized corrosion (MK2_1 corroded more severely than MK2_2). In the S3a-661 mortar, one sensor (S3a-661_1) showed no corrosion throughout the whole period of exposure, whereas S3a-661_2 started to corrode in the latter stages of the exposure (after 42 weeks; Fig. 8a). Although the general corrosion rate was mild, a major shift developed in a very short time. Based on these responses, it can be concluded that, in the S3a-661 mortar, only one or very few pits were generated in a very short time, in a mainly passive environment. A similar process might have occurred on the S3a-661_2 sensor as well, but the exposure duration was likely too short to affect the electrical resistance of the sensor. In all cases, the microCT scans of the ER sensors were in agreement with the measurements.

The reinforcement embedded in the AAM mortars showed a mixed pattern of corrosion damage, with some areas exhibiting individual pits and others more general corrosion (Fig. 8c). The actual damage on the reinforcement can be roughly correlated to the ER sensor measurements, although some differences could also be observed. These differences could be attributed to the predominantly localized corrosion, which cannot be measured by ER sensors during the initiation phase. Estimated parameters of the damage on specific reinforcements are presented in Table 4. In the FA8 (fly ash) mortar the reinforcement exhibited mild general corrosion, in combination with minor localized corrosion. The MK2 (metakaolin) mortar represents the worst corrosion environment in terms of both aspects, exhibiting the highest general corrosion and significant localized corrosion, as well as the largest areas either heavily (depths >0.5 mm) or mildly corroded. The S3a-661 (slag) mortar exhibited the best resistance to general corrosion, but the

Table 4
Estimation of the corrosion damage on steel rebars (Φ14) exposed to different AAM mortars for up to 67 weeks.

	AVERAGE diameter (mm)	CHANGE in diameter (μm)	GENERAL v_{corr} (μm/year)	MAX pit depth (mm)	MAX LOCAL v_{corr} (μm/year)	CORRODED AREA (%)	HEAVILY corroded area >0.5 mm (%)	MILDLY corroded area (%)
FA8-5	14.21	88	78	-0.5	460	1	0	1
MK2-3	14.16	137	121	-0.9	796	5	3	2
S3a-661-1	14.22	78	69	-1.2	1044	1	0	1

reinforcement suffered from rather deep pits.

4.3. Comparison of results

Although some differences were observed between the implemented techniques, the results were largely compatible and provided a comprehensive picture of the corrosion processes. The ER sensors offered reliable data on general corrosion rates over time. Discrepancies between the estimated cumulative corrosion damage measured by ER sensor and the actual damage observed in rebars embedded in AAM mortars were primarily attributed to localized corrosion. Unlike ER sensors, which are relatively insensitive to pitting corrosion until the pit dimensions significantly affect the sensor's cross-section, the CMEA technique was capable of detecting corrosion initiation and the spatial distribution of anodic and cathodic sites, making it more suitable for monitoring localized corrosion. In addition to the differing characteristics of the ER and CMEA techniques, which undoubtedly contributed to some variability in the results, the disparity in experimental duration (66 weeks vs. 29 weeks) likely introduced further differences. Nevertheless, both sets of results clearly demonstrated the evolving nature of the corrosion processes—not only in terms of general corrosion rates but also with respect to the type of corrosion observed—thus making direct comparison through extrapolation questionable.

One possible source of the discrepancies between the results is the difference in surface conditions between the CMEA and the ER sensors (polished and etched surfaces) compared to the reinforcement (as-received surface conditions with an oxide layer). It was found that the steel microstructure can affect not only the initiation of corrosion but to some extent, the corrosion rate [47,48]. According to our previous study [23], these differences can be even more pronounced when comparing the corrosion in pore solutions and solid mortars, with the effect being more evident in an AAM environment than in OPC materials. However, the main differences are likely related to the steel–concrete interface (SCI), which is also influenced by surface conditions. While the SCI has been shown to play a key role in the initiation and evolution of corrosion processes in cementitious materials [41,42,50], it remains largely unstudied in AAM mortars. In any case, due to inherent differences in structure and dimensions, working electrodes and corrosion sensors used in tests can never fully replicate the conditions of real reinforcing steel, and such discrepancies cannot be entirely avoided.

As mentioned in the Introduction, several studies on steel corrosion in AAMs have been published [18–21], but they typically do not address the relationship between electrochemical parameters and the specific corrosion characteristics (type and evolution) [18,19] discussed in this study. However, our findings suggest that the complexity of the problem, particularly the non-stationary spatio-temporal nature of the corrosion processes, may be even greater in AAMs than in conventional cementitious materials. As a result, wider generalization of the obtained results was not possible. Nevertheless, these findings could serve as a foundation for future research, focusing on the spatiotemporal characteristics of corrosion in closer relation to the structural and chemical properties of individual AAMs. To address this, narrowing the selection of AAM mortars and prolonging the exposure period could be a reasonable approach for future studies.

5. Conclusions

The findings of this study provide valuable insights into the corrosion behavior of steel embedded in various alkali-activated mortars (AAMs) based on fly ash (FA8), metakaolin (MK2), and slag (S3a-661). Two advanced corrosion monitoring techniques, coupled multi-electrode array (CMEA) and electrical resistance (ER) sensors, were employed for long-term monitoring. The results obtained from these techniques were complemented by a damage assessment using X-ray computed microtomography (microCT) imaging. The following conclusions were drawn:

- In the fly ash-based AAM mortar (FA8), mild general corrosion was found with pitting corrosion in certain areas. The metakaolin-based AAM mortar (MK2) induced the worst corrosion damage, which consisted of intensive general corrosion as well as significant localized corrosion. In the slag-based AAM mortar (S3a-661) only minor overall corrosion was observed; however, some deep pits were detected, indicating the highest maximum local corrosion rate.
- In addition to indicating the initiation time, the measurements with ER sensors provided reliable information on general corrosion rates over time. Based on the evolution of these corrosion rates, the type of corrosion (local vs. general) was also determined.

- The CMEA method effectively measured corrosion initiation and spatiotemporal distribution of the anodic and cathodic sites. In all of the mortars, the anodic (corrosion) current was limited to a few electrodes, while the cathodic current was more widely distributed among the electrodes. The highest corrosion rate, as well as the highest cumulative amount of corrosion damage, was detected in the metakaolin-based AAM mortar (MK2). Intensive localized corrosion processes were also observed in the slag-based AAM mortar (S3a-661), while the CMEA measurements in the fly ash-based AAM mortar (FA8) indicated moderate corrosion activity.

Based on the compatible results obtained using advanced techniques (CMEA and ER sensors), this study provided valuable insights into steel corrosion in selected alkali-activated materials (AAMs). The findings highlight the complexity of corrosion processes, particularly their dynamic behavior over time and space. Differences in corrosion mechanisms between various AAM systems appear to be even more pronounced than those observed in blended cements, indicating that corrosion behavior cannot be generalized across all AAMs. Future research should therefore closely link the temporal and spatial characteristics of corrosion processes to the specific structural and chemical properties of each AAM formulation. A long-term experimental approach is also considered essential to fully capture the evolving nature of corrosion in these systems.

CRediT authorship contribution statement

Nina Gartner: Writing – original draft, Investigation, Formal analysis, Conceptualization. **Tadeja Kosec:** Writing – review & editing, Supervision, Formal analysis, Conceptualization. **Miha Hren:** Investigation, Formal analysis. **Andraž Legat:** Writing – review & editing, Supervision, Funding acquisition.

Funding

The authors gratefully acknowledge the financial support of the Slovenian Research and Innovation Agency (ARIS) through the research program P2–0273, “Building Structures and Materials.”

Declaration of Competing Interest

The authors declare that they have no known competing financial interests or personal relationships that could have appeared to influence the work reported in this paper.

Acknowledgements

The authors gratefully acknowledge their colleagues at the Laboratory for Metals, Corrosion and Anti-Corrosion Protection for their support. They also thank Dr. Vilma Ducman and her team at the Laboratory for Cements, Mortars, and Ceramics, ZAG, for their assistance with the selection and preparation of alkali-activated mortar specimens.

Appendix A. Supporting information

Supplementary data associated with this article can be found in the online version at doi:10.1016/j.cscm.2025.e05165.

Data Availability

The research data supporting the findings of this study have been deposited in the DiRROS repository, accessible at http://hdl.handle.net/20.500.12556/DiRROS-22557.

References

[1] K.L. Scrivener, R.J. Kirkpatrick, Innovation in use and research on cementitious material, Cem. Concr. Res. 38 (2008) 128–136, https://doi.org/10.1016/j.cemconres.2007.09.025.
[2] J.S.J. Van Deventer, Chapter 10 - progress in the adoption of geopolymer cement, in: A. Nazari, J.G. Sanjayan (Eds.), Handbook of Low Carbon Concrete, Butterworth-Heinemann, Oxford, UK, 2017, pp. 217–262, https://doi.org/10.1016/B978-0-12-804524-4.00010-5.
[3] J.L. Provis, S.A. Bernal, Geopolymers and related alkali-activated materials, Annu. Rev. Mater. Res. 44 (2014) 299–327, https://doi.org/10.1146/annurev-matsci-070813-113515.
[4] J.L. Provis, Alkali-activated materials, Cem. Concr. Res. 114 (2018) 40–48, https://doi.org/10.1016/j.cemconres.2017.02.009.
[5] C. Shi, D. Roy, P. Krivenko, Alkali-activated cements and concretes, CRC Press, Taylor & Francis, London, UK, 2006.
[6] D.L.Y. Kong, J.G. Sanjayan, Effect of elevated temperatures on geopolymer paste, mortar and concrete, Cem. Concr. Res. 40 (2010) 334–339, https://doi.org/10.1016/j.cemconres.2009.10.017.
[7] A.M.M.A. Bakri, H. Kamarudin, M. Binhussain, I.K. Nizar, A.R. Rafiza, Y. Zarina, Comparison of geopolymer Fly ash and ordinary portland cement to the strength of concrete, Adv. Sci. Lett. 19 (2013) 3592–3595, https://doi.org/10.1166/asl.2013.5187.
[8] E. Ofer-Rozovsky, M.A. Haddad, G. Bar-Nes, E.J.C. Borojovich, A. Binyamini, A. Nikolski, A. Katz, Cesium immobilization in nitrate-bearing metakaolin-based geopolymers, J. Nucl. Mater. 514 (2019) 247–254, https://doi.org/10.1016/j.jnucmat.2018.11.003.

[9] Z. Ma, B. Wang, Z. Zhang, Y. Zhang, C. Wang, New insights into the effects of silicate modulus, alkali content and modification on multi-properties of recycled brick powder-based geopolymer, J. Build. Eng. 97 (2024) 110989, https://doi.org/10.1016/j.jobe.2024.110989.

[10] Z. Ma, Y. Wu, K. Fang, Y. Zhang, C. Wang, Developing fully recycled alkali-activated mortar made with waste concrete fines as a substitute for both binder and sand: Multi-properties evaluation, Constr. Build. Mater. 477 (2025) 141323, https://doi.org/10.1016/j.conbuildmat.2025.141323.

[11] C. Wang, J. Liu, B. Lu, Y. Zhang, Z. Ma, Stiffness degradation and mechanical behavior of microfiber-modified high-toughness recycled aggregate concrete under constant load cycling, Eng. Fract. Mech. 312 (2024) 110608, https://doi.org/10.1016/j.engfracmech.2024.110608.

[12] C. Wang, J. Yuan, Y. Zhang, Z. Ma, Study on the mesoscopic mechanical behavior and damage constitutive model of micro-steel fiber reinforced recycled aggregate concrete, Constr. Build. Mater. 443 (2024) 137767, https://doi.org/10.1016/j.conbuildmat.2024.137767.

[13] C. Alonso, C. Andrade, J.A. González, Relation between resistivity and corrosion rate of reinforcements in carbonated mortar made with several cement types, Cem. Concr. Res. 18 (1988) 687–698, https://doi.org/10.1016/0008-8846(88)90091-9.

[14] G.K. Glass, C.L. Page, N.R. Short, Factors affecting the corrosion rate of steel in carbonated mortars, Corros. Sci. 32 (1991) 1283–1294, https://doi.org/10.1016/0010-938X(91)90048-T.

[15] M. Criado, J.L. Provis, Alkali activated slag mortars provide high resistance to Chloride-Induced corrosion of steel, Front. Mater. 5 (2018), https://doi.org/10.3389/fmats.2018.00034.

[16] T. Huyen Vu, L.C. Dang, G. Kang, V. Sirivivatnanon, Chloride induced corrosion of steel reinforcement in alkali activated slag concretes: a critical review, Case Stud. Constr. Mater. 16 (2022) e01112, https://doi.org/10.1016/j.cscm.2022.e01112.

[17] S. Mundra, G. Samson, G. Masi, R. Achenbach, D.M. Bastidas, S.A. Bernal, M.C. Bignozzi, M. Criado, M. Cyr, N. Gartner, S. von Greve-Dierfeld, A. Legat, A. Nikoonasab, J.L. Provis, M. Raupach, G.J.G. Gluth, Application of electrochemical methods for studying steel corrosion in alkali-activated materials, Mater. Corros. 74 (2023) 988–1008, https://doi.org/10.1002/maco.202313743.

[18] A. Runci, J.L. Provis, M. Serdar, Revealing corrosion parameters of steel in alkali-activated materials, Corros. Sci. 210 (2023) 110849, https://doi.org/10.1016/j.corsci.2022.110849.

[19] J. Shi, J. Ming, W. Sun, Electrochemical performance of reinforcing steel in alkali-activated slag extract in the presence of chlorides, Corros. Sci. 133 (2018) 288–299, https://doi.org/10.1016/j.corsci.2018.01.043.

[20] X. Xu, X. Hu, A. Khaskhoussi, C. Shi, Passivation and depassivation of reinforcement steel in alkali-activated materials—A review, Cem. Concr. Compos. 154 (2024) 105802, https://doi.org/10.1016/j.cemconcomp.2024.105802.

[21] X. Zhou, Z. Geng, J. Shi, Enhanced passivity of reinforcing steel in cementitious materials with thermally-activated red mud, Cem. Concr. Compos. 153 (2024) 105696, https://doi.org/10.1016/j.cemconcomp.2024.105696.

[22] N. Gartner, M. Hren, T. Kosec, A. Legat, Characterizing steel corrosion in different alkali-activated mortars, Materials 14 (2021) 7366, https://doi.org/10.3390/ma14237366.

[23] N. Gartner, T. Kosec, S. Poyet, A. Legat, The corrosion properties of steel in pore solutions obtained from alkali-activated mortars, Mater. Corros. 74 (2023) 1009–1021, https://doi.org/10.1002/maco.202313729.

[24] Ø. Vennesland, M. Raupach, C. Andrade, Recommendation of rilem TC 154-EMC: "Electrochemical techniques for measuring corrosion in concrete"—measurements with embedded probes, Mater. Struct. 40 (2007) 745–758, https://doi.org/10.1617/s11527-006-9219-4.

[25] A. Fahim, P. Ghods, O.B. Isgor, M.D.A. Thomas, A critical examination of corrosion rate measurement techniques applied to reinforcing steel in concrete, Mater. Corros. (2018), https://doi.org/10.1002/maco.201810263.

[26] A. Česen, T. Kosec, A. Legat, Characterization of steel corrosion in mortar by various electrochemical and physical techniques, Corros. Sci. 75 (2013) 47–57, https://doi.org/10.1016/j.corsci.2013.05.015.

[27] A. Legat, Monitoring of steel corrosion in concrete by electrode arrays and electrical resistance probes, Electrochim. Acta 52 (2007) 7590–7598, https://doi.org/10.1016/j.electacta.2007.06.060.

[28] M. Hren, V. Bokan Bosiljkov, A. Legat, Effects of blended cements and carbonation on chloride-induced corrosion propagation, Cem. Concr. Res. 145 (2021) 106458, https://doi.org/10.1016/j.cemconres.2021.106458.

[29] M. Hren, T. Kosec, A. Legat, Characterization of stainless steel corrosion processes in mortar using various monitoring techniques, Constr. Build. Mater. 221 (2019) 604–613, https://doi.org/10.1016/j.conbuildmat.2019.06.120.

[30] T. Kosec, A. Kranjc, B. Rosborg, A. Legat, Post examination of copper ER sensors exposed to bentonite, J. Nucl. Mater. 459 (2015) 306–312, https://doi.org/10.1016/j.jnucmat.2015.01.058.

[31] A. Legat, M. Leban, Ž. Bajt, Corrosion processes of steel in concrete characterized by means of electrochemical noise, Electrochim. Acta 49 (2004) 2741–2751, https://doi.org/10.1016/j.electacta.2004.01.036.

[32] L. Mariaca, A. Bautista, P. Rodríguez, J.A. González, Use of electrochemical noise for studying the rate of corrosion of reinforcements embedded in concrete, Mat. Struct. 30 (1997) 613–617, https://doi.org/10.1007/BF02486903.

[33] L. Yang (Ed.), Techniques for Corrosion Monitoring, Woodhead Publishing and Maney Publishing on behalf of The Institute of Materials, Minerals & Mining, Cambridge England, 2008.

[34] U.M. Angst, E. Rossi, C.B. Käthler, D. Mannes, P. Trtik, B. Elsener, Z. Zhou, M. Strobl, Chloride-induced corrosion of steel in concrete – insights from bimodal neutron and X-ray microtomography combined with ex-situ microscopy, (2023). ⟨https://doi.org/10.48550/arXiv.2307.10261⟩.

[35] M. Hren, T. Kosec, A. Legat, Characterization of steel corrosion processes in various blended cements by means of coupled multi-electrode arrays, Cem. Concr. Res. 168 (2023) 107134, https://doi.org/10.1016/j.cemconres.2023.107134.

[36] J.L. Provis, K. Arbi, S.A. Bernal, D. Bondar, A. Buchwald, A. Castel, S. Chithiraputhiran, M. Cyr, A. Dehghan, K. Dombrowski-Daube, A. Dubey, V. Ducman, G.J.G. Gluth, S. Nanukuttan, K. Peterson, F. Puertas, A. van Riessen, M. Torres-Carrasco, G. Ye, Y. Zuo, RILEM TC 247-DTA round robin test: mix design and reproducibility of compressive strength of alkali-activated concretes, Mater. Struct. 52 (2019) 99, https://doi.org/10.1617/s11527-019-1396-z.

[37] G.J.G. Gluth, K. Arbi, S.A. Bernal, D. Bondar, A. Castel, S. Chithiraputhiran, A. Dehghan, K. Dombrowski-Daube, A. Dubey, V. Ducman, K. Peterson, P. Pipilikaki, S.L.A. Valcke, G. Ye, Y. Zuo, J.L. Provis, RILEM TC 247-DTA round robin test: carbonation and chloride penetration testing of alkali-activated concretes, Mater. Struct. 53 (2020) 21, https://doi.org/10.1617/s11527-020-1449-3.

[38] F. Winnefeld, G.J.G. Gluth, S.A. Bernal, M.C. Bignozzi, L. Carabba, S. Chithiraputhiran, A. Dehghan, S. Dolenec, K. Dombrowski-Daube, A. Dubey, V. Ducman, Y. Jin, K. Peterson, D. Stephan, J.L. Provis, RILEM TC 247-DTA round robin test: sulfate resistance, alkali-silica reaction and freeze–thaw resistance of alkali-activated concretes, Mater. Struct. 53 (2020) 140, https://doi.org/10.1617/s11527-020-01562-0.

[39] G. Gluth, W. Rickard, Design and characterization of fly ash-based geopolymer concretes for a round-robin durability testing program, in: C. Leonelli, M. Romagnoli (Eds.), Geopolymers: The Route to Eliminate Waste and Emissions in Ceramic and Cement Manufacturing, Engineering Conferences International / Società Ceramica Italiana, Hernstein, Austria, 2015: pp. 67–70. ⟨https://opus4.kobv.de/opus4-bam/frontdoor/index/index/docId/33106⟩ (accessed February 17, 2021).

[40] K.D. Ralston, N. Birbilis, C.H.J. Davies, Revealing the relationship between grain size and corrosion rate of metals, Scr. Mater. 63 (2010) 1201–1204, https://doi.org/10.1016/j.scriptamat.2010.08.035.

[41] U.M. Angst, M.R. Geiker, A. Michel, C. Gehlen, H. Wong, O.B. Isgor, B. Elsener, C.M. Hansson, R. François, K. Hornbostel, R. Polder, M.C. Alonso, M. Sanchez, M. J. Correia, M. Criado, A. Sagüés, N. Buenfeld, The steel–concrete interface, Mater. Struct. 50 (2017) 143, https://doi.org/10.1617/s11527-017-1010-1.

[42] U.M. Angst, M.R. Geiker, M.C. Alonso, R. Polder, O.B. Isgor, B. Elsener, H. Wong, A. Michel, K. Hornbostel, C. Gehlen, R. François, M. Sanchez, M. Criado, H. Sørensen, C. Hansson, R. Pillai, S. Mundra, J. Gulikers, M. Raupach, J. Pacheco, A. Sagüés, The effect of the steel–concrete interface on chloride-induced corrosion initiation in concrete: a critical review by RILEM TC 262-SCI, Mater. Struct. 52 (2019) 88, https://doi.org/10.1617/s11527-019-1387-0.

[43] T. Kosec, V. Kuhar, A. Kranjc, V. Malnarič, B. Belingar, A. Legat, Development of an electrical resistance sensor from high strength steel for automotive applications, Sensors 19 (2019) 1956, https://doi.org/10.3390/s19081956.

[44] R.G. Kelly, J.R. Scully, D.W. Shoesmith, R.G. Buchheit, Electrochemical techniques in corrosion science and engineering, Marcel Dekker, Inc, New York, NY, USA, 2003. ⟨https://www.academia.edu/14723973/Electrochemical_Techniques_in_Corrosion_Science_and_Engineering⟩ (accessed January 13, 2020).

[45] C. Alonso, C. Andrade, M. Castellote, P. Castro, Chloride threshold values to depassivate reinforcing bars embedded in a standardized OPC mortar, Cem. Concr. Res. 30 (2000) 1047–1055, https://doi.org/10.1016/S0008-8846(00)00265-9.
[46] C. Andrade, C. Alonso, Test methods for on-site corrosion rate measurement of steel reinforcement in concrete by means of the polarization resistance method, Mat. Struct. 37 (2004) 623–643, https://doi.org/10.1007/BF02483292.
[47] A. Česen, T. Kosec, A. Legat, V. Bokan-Bosiljkov, Corrosion properties of different forms of carbon steel in simulated concrete pore water, Mater. Tehnol. 48 (2014) 51–57.
[48] M. Stefanoni, U. Angst, B. Elsener, Local electrochemistry of reinforcement steel – distribution of open circuit and pitting potentials on steels with different surface condition, Corros. Sci. 98 (2015) 610–618, https://doi.org/10.1016/j.corsci.2015.06.004.
[49] N. Gartner, T. Kosec, A. Legat, Monitoring the corrosion of steel in concrete exposed to a marine environment, Materials 13 (2020) 407, https://doi.org/10.3390/ma13020407.
[50] M. Hren, T. Kosec, A. Legat, An investigation into corrosion around voids at the steel-concrete interface, Cem. Concr. Res. 181 (2024) 107545, https://doi.org/10.1016/j.cemconres.2024.107545.

Glossary

AAM: alkali-activated material/mortar
CLI: corrosion localization index
CMEA sensor: coupled multi-electrode array sensor
D: total corrosion damage depth
D_V: total corrosion damage volume
EN: electrochemical noise
ER sensor: electrical resistance sensor
FA: fly-ash
FA8: fly-ash based AAM
j_{cath}: real-time cathodic current density
$j_{cath\text{-}AVERAGE}$: average cathodic current density
j_{corr}: real-time anodic current density
j_{corr}-*AVERAGE:* average (local) anodic current density
j_{corr}-*AVERAGE-max:* maximum average anodic current density
$j_{corr\text{-}GENERAL}$: general anodic (corrosion) current density
j_{RT}: real-time current density
microCT: X-ray computed microtomography
MK: metakaolin
MK2: metakaolin based AAM
ν_{corr}: real-time corrosion rate
$\nu_{corr\text{-}AVERAGE}$: average corrosion rate
$\nu_{corr\text{-}AVERAGE\text{-}max}$: highest average (local) corrosion rate
$\nu_{corr\text{-}GENERAL}$: general corrosion rate
OPC: ordinary Portland cement
S3a-661: steel slag based AAM
SCM: supplementary cementitious material
ZRA: zero-resistance ammeter